Potential energy surfaces for Ir+H2 and Ir++H2 reactions

K. Balasubramanian and Dingguo Dai

Citation: J. Chem. Phys. **93**, 7243 (1990); doi: 10.1063/1.459447
View online: http://dx.doi.org/10.1063/1.459447
View Table of Contents: http://jcp.aip.org/resource/1/JCPSA6/v93/i10
Published by the American Institute of Physics.

Potential energy surfaces for $Ir + H_2$ and $Ir^+ + H_2$ reactions

K. Balasubramanian[a] and Dingguo Dai
Department of Chemistry, Arizona State University, Tempe, Arizona 85287-1604

(Received 16 July 1990; accepted 1 August 1990)

Potential energy surfaces of 10 electronic states of IrH_2 and 12 electronic states of IrH_2^+ are computed. A complete active space multi-configuration self-consistent field (CAS-MCSCF) followed by multireference configuration interaction (MRCI) calculations which included up to 270 000 configurations are employed. In addition spin–orbit effects are studied using the relativistic configuration interaction (RCI) method. It is found that the $Ir(^2F)$ state inserts spontaneously into H_2 to form a stable IrH_2 molecule in a $^2A_1$ ground state which is 28 kcal/mol more stable than $Ir(^4F) + H_2$ in the absence of spin–orbit effects. The spin–orbit coupling of the quartet and doublet states provides nonzero transition probability for the insertion of Ir (^4F) state into H_2. The ^3P state of Ir^+ was found to insert spontaneously into H_2 to form the $^3A_2$ ground state of IrH_2^+ which is 30 kcal/mol more stable than $Ir^+(^5D) + H_2$. An excited singlet state of Ir^+ also was found to insert into H_2 spontaneously. The spin–orbit couplings of quintet and triplet states of IrH_2^+ at the crossing of these curves provide nonzero transition probability for the insertion of Ir^+ (^5D) into H_2. The bent E ground state of IrH_2 in the C_{2v}^2 group was found to be a 63% $^2A_1$, 16% $^2B_1$ and 17% $^2A_2$ mixture. This strong mixing induces a large H–Ir–H bond angle change of 9.5° in the E(III) state of IrH_2. The $^3A_2$ (A_1) ground state of IrH_2^+ was found to be a 63% $^3A_2$, 15% $^3B_2$, 12% $^3B_1$ and 7% $^1A_1$ mixture. This strong spin–orbit mixing induces a θ_e change of almost 9° in the ground state of IrH_2^+. The adiabatic ionization potential including spin–orbit effects for IrH_2 and Ir are calculated as 8.2 and 8.6 eV, respectively. The ground state of IrH_2 was found to be ionic ($\mu_e = 2.2$ D) with Ir^+H^- polarity exhibiting $Ir(6s^{0.75}6p^{0.12}5d^{8.06})$ hybridization. The IrH_2^+ ion in its $^3A_2$ state exhibits $Ir^+(6s^{0.62}6p^{0.12}5d^{7.51})$ hybridization character.

I. INTRODUCTION

The reactivity pattern of transition metal clusters and their ions with small molecules such as H_2 are the topics of several experimental and theoretical studies in recent years.[1–16] In particular, gas phase reactions of transition metal atoms and ions with H_2 have been studied experimentally quite extensively.[2,3,5,6] The reactivities of transition metal clusters in dissociative chemisorption with H_2 are found to vary dramatically with cluster size.[1,7–9] For example, Fe, Nb and Co clusters exhibit strong size dependency while Ni clusters do not exhibit such a variation.

Beauchamp, Armentrout and their co-workers[2,5,6] have studied the energetics and dynamics of the reactions of single transition metal atoms and ions with H_2 as well as CH_4. The M–H, $M–H^+$, $M–CH_3$ as well as $M–CH_3^+$ bond energies for several transition metal atoms have been measured using these experiments. Knight, Weltner and co-workers and other authors,[4,10] have used the rare gas matrix isolation electron spin resonance (ESR) techniques and gas phase–phase techniques to investigate the reactivities of species such as $Pd^+ + H_2$ as well as transition metal hydrides such as PdH, MnH, etc. All of these studies have resulted in a wealth of information.

Theoretical studies of MH_2 and MH_2^+ species for the transition metal atoms are now restricted to the first two row transition metal atoms with the exception of PtH_2 which has been studied extensively both in our lab and by other investigators.[15] Similarly, AuH_2 has been studied.[16] Such studies have revealed considerable electronic state dependencies on the reactivities. In general, low spin electronic states of the metal atoms insert into H_2 forming stable bent MH_2 species while the high spin state of the metal atoms often have to surmount large barriers for insertion into H_2. For example, theoretical calculations on TcH_2 and RuH_2[25] have revealed that $Tc(^6S)$ atom has to surmount a large barrier for insertion into H_2 while an excited doublet state inserts into H_2 spontaneously. Similarly, the ^5F state of Ru atom has to surmount a large barrier for insertion into H_2 while the excited ^3F and ^1G states insert into H_2.[25] A recent study on TcH_2^+ and RuH_2^+[17] revealed that Tc^+ ($a\,^7S$) state has to surmount a large barrier while a low-lying excited Tc^+ ($a\,^5D$) state inserts into H_2 spontaneously. To the contrary Ru^+ in its ^{4}F ground state readily inserts into H_2. Such theoretical studies also have provided considerable insight into the nature of M–H bonds, the role of d orbitals in these bonds and in the dissociative chemisorptive process, the stability of MH_2, etc.

The IrH_2 and RhH_2 moieties[18–22] are found in hydroborate complexes or by chelation of diphosphine complexes. Eisenberg and Fisher[18] mention that no set of complexes in catalytic activation of substrates have been more vigorously studied in the last two decades than those of Rh and Ir. The complexes of both Rh and Ir in d^8 ionic states possess rich electron density and thus oxidation chemistry. Both Ir and Rh are important materials in catalysis. Experimentally it is known that electron richness of Ir yields considerably more stable complexes. Crabtree *et al.*[19] have also studied several Ir dihydride and trihydride complexes.

[a] Camille and Henry Dreyfus Teacher–Scholar.

There are no accurate *ab initio* calculations including relativistic and electron correlation effects for IrH_2 and IrH_2^+ species at present. The objective of this study is to investigate the potential energy surfaces of IrH_2 and IrH_2^+ arising from both the ground state and low-lying excited states of Ir and Ir^+ with the intent of juxtaposing the reactivity of different states of Ir and Ir^+ with H_2. We employ complete active space MCSCF (CAS/MCSCF followed by multireference CI (MRCI) calculations which included up to 270 000 configurations. In addition spin–orbit effects are studied using the relativistic CI (RCI) method. We employ a large (5*s*5*p*4*d*) semicore and valence Gaussian basis for Ir.

II. METHOD OF COMPUTATION

We employed a complete active space multiconfiguration self-consistent field (CAS-MCSCF) method to generate the orbitals for higher order MRCI calculations. Both CAS-MCSCF and MRCI calculations were made using relativistic effective core potentials (RECPs) which retained the outer $5s^25p^65d^76s^2$ shells of the Ir atom in the valence space. Ross *et al.*[23] have generated such RECPs including the spin–orbit coupling term for the Ir atom. We start with their (5*s*5*p*3*d*) basis set. The first two large exponents *s* and *p* functions are for describing the 5*s* and 5*p* orbitals of Ir atom and to yield nodal structures for the 6*s* and 6*p* orbitals. The diffuse exponents in the 5*p* basis used here also generate the 6*p* orbital of Ir which hybridizes with 5*d* and 6*s* near the bending region. Our starting 5*d* basis set is triplet-zeta in quality. To this are added another set of diffuse six component *d* functions with $\alpha_d = 0.0552$. In earlier studies on several second row MH_2 species the effect of 10 component 4*f* functions were tested. It was established that these functions change bond lengths by only 0.001–0.003 Å. Consequently, in the present study the 4*f* functions were not included since it is evident that the effect of these functions is rather small. Our final basis thus consisted of a (5*s*5*p*4*d*) Gaussian basis set.

The IrH_2 and IrH_2^+ species were oriented on the *YZ* plane with the *z* axis bisecting the H–Ir–H bond angle. In the CAS-MCSCF calculations we included all orbitals of Ir and H which correlated into Ir (6*s*), Ir (5*d*) and H (1*s*) orbitals at infinite separation. In the C_{2v} symmetry this active space comprised four a_1 orbitals, two b_2 orbitals and one each of b_1 and a_2 symmetries. Then the outer 11 electrons of IrH_2 and 10 electrons of IrH_2^+ were distributed in all possible ways among the eight active orbitals described above. Thus CAS-MCSCF calculations were made in a full CI space of valence electrons and valence orbitals. The 5*s* and 5*p* semicore orbitals were allowed to relax at the CAS-MCSCF but no excitations from these orbitals were allowed.

We used a multireference singles + doubles CI (MRCI) method to include the effect of higher-order electron correlation effects not included in the zeroth-order CAS/MCSCF method. The MRCI calculations included single + double excitations from all configurations in the CAS-MCSCF wave functions with coefficients $\geqslant 0.07$. Separate CAS-MCSCF calculations were made for each state of different spatial symmetry in C_{2v} or spin multiplicity. Our CAS-MCSCF calculations of IrH_2 included up to 264 CSFs while MRCI calculations included up to 270 000 configurations. Similarly, the CAS-MCSCF of IrH_2^+ included up to 384 CSFs while MRCI calculations include up to 200 000 configurations.

The spin–orbit splitting of the Ir atom is known to be large. We included the effect of spin–orbit term using a relativistic configuration interaction method described before by one of the authors.[26] The RCI calculations were made near the potential wells of three low-lying doublet states of IrH_2 and at the crossings of bending potential energy surfaces of quartet and doublet states. These calculations were carried out in the C_{2v}^2 double group. For example, the $^2A_1$ state near its θ_e with a leading configuration open shell spin of α included in the RCI, reference configurations for a $^2B_1$ state with open shell spin β, $^2A_2$ state with spin α and a $^2B_2$ state in the spin β. In addition a few quartet states with appropriate spin function combinations in the C_{2v}^2 double group were included. Subsequently, single and double excitations were included in the RCI. The same set of calculations was repeated without the spin–orbit integrals. The differences in the energies and geometries were then applied as corrections to the CAS/MRCI results.

The RCI calculations made at the quartet–doublet curve-crossing included all possible quartet states with appropriate spin function combinations and the $^2A_1$ state with the objective of studying the transition probability for the quartet to doublet nonadiabatic transition at curve crossings.

The RCI calculations of IrH_2^+ were made on the spin–orbit states arising from the $^3A_2$, $^3B_1$ and $^3B_2$ states. The $^3A_2$ state correlates into A_1, B_2 and B_1 states in the C_{2v}^2 double group. The $^3B_1$ state correlates into A_1, B_2, and A_2 symmetries while the $^3B_2$ state gives rise to A_1, B_1 and A_2 symmetries. Pitzer and Winter[27] have worked out the appropriate symmetry-adapted spin functions in the C_{2v}^2 double group. All nine spin–orbit states of IrH_2^+ were studied here. The RCI calculations of the A_1 state included all low-lying reference configurations in the C_{2v}^2 double group which have the A_1 symmetry. The RCI calculations include up to 26 reference configurations and single + double excitations from these configurations.

The RCI calculations at the crossings of triplet and quintet states included all possible quintet states with appropriate spin function combination for a given triplet state correlating into a spin–orbit state in C_{2v}^2.

All CAS-MCSCF/MRCI calculations were made using one of the author's[29] modified versions of ALCHEMY II codes[28] to include RECPs. The RCI calculations were done using the general RCI method for polyatomics described in Ref. 26. The spin–orbit integrals for the RCI were obtained using Pitzer's ARGOS integral codes.[30] It should be mentioned that Hay and Wadt[31] have also generated RECPs for Ir which work satisfactorily except for the spin–orbit effects which are not included in the Hay–Wadt ECPs.

III. RESULTS AND DISCUSSION

A. Energy separations of Ir and Ir^+

Table I shows our computed energy separations of pertinent quartet and doublet states of Ir and ^5D, ^3F and ^1G states

TABLE I. Atomic energy separations of Ir and Ir^+ obtained from asymptotic molecular energy separations at the dissociation limit.

Configuration	Atomic state	$E(cm^{-1})$ Theory	$E(cm^{-1})$ Expt.[a]
$5d^76s^2$	Ir (^4F)	0	0
$5d^86s^1$	Ir (^2F)	9195	9086
$5d^76s^1$	Ir^+ (^5D)	0	...
	Ir^+ (^3F)	4442	...
	Ir^+ (^1G)	11171	...

[a] J-weighted average energy separation from Ref. 32. Our theoretical IP of Ir is 8.6 eV compared to an experimental value of 9 eV in Ref. 32.

of Ir^+. As seen from Table I, the ground state of Ir is a ^4F state arising from the $5d^76s^2$ configuration in agreement with established experimental atomic spectra.[32] The ^2F excited state arising from $5d^86s^1$ state is computed at $\sim$9195 cm^{-1} while the corresponding J-weight atomic separation from Moore's Table is $\sim$9086 cm^{-1}. Note that there is a low-lying Ir (^2P) state arising from the same configuration[32] but we believe that the state to which doublet states of IrH_2 dissociate is Ir (^2F) since four PES go to the same limit and a $^2\Phi_u$ state goes to this limit.

The ionization potential of Ir atom is calculated as 7.1 eV at the CAS-MCSCF level and 8.3 eV at the MRCI level. The spin–orbit correction to the more accurate MRCI result yields an IP of 8.6 eV compared to an experimental IP of 9 eV.[32] Therefore the energy separations of IrH_2 relative to IrH_2^+ are not as well computed as the energy separations of neutral states or the energy separations of different states of IrH_2^+ relative to the ground state of IrH_2^+.

There are no atomic spectral data listed in Moore's Tables for Ir^+.[32] Our theoretical calculations predict the quintet states of IrH_2^+ dissociate to Ir^+ in the ($5d^76s^1$) configuration. For some states ($5d^76s^1$) and ($5d^66s^2$) mixing was found. The ground state of the isoelectric atom is ($5d^66s^2$) ^5D. Since $5d^66s^2$–$5d^76s^1$ mixing was found we assign the Ir^+ state as ^5D. Ir^+ ^5D–^3F separation for our asymptotic separation at the dissociation limit is computed as $\sim$4400 cm^{-1} while the Ir^+ ^5D–^1G separation is calculated as 11 200 cm^{-1}.

B. IrH_2

1. Potential energy surfaces of IrH_2

Figure 1 shows the bending PES of ten electronic states of doublet, quartet and sextet spin multiplicities. The quartet states of IrH_2 arise from the Ir (^4F) ground state with the electronic configuration $5d^76s^2$ (see Table I). The doublet states correlate into Ir (^2F) arising from the $5d^86s^1$ configuration. Note that the assignment to Ir (^2F) is based on the fact that a linear doublet state of IrH_2 correlates into $^2\Phi_u$ and thus the angular momentum of the atomic state must be at least three. This is the most compatible atomic state with $5d^86s^1$ configuration in this region. The sextet states are most interesting in that they correlate into Ir (b^4F) + H(^2S) + H(^2S). Consequently, the energy separations of quartet and sextet states at the dissociation limit correspond to the D_e of H_2. The sextet states are bound with respect to Ir (^4F) + H + H as anticipated.

Table II shows the equilibrium geometries of the bent electronic states of IrH_2 at both the CAS-MCSCF and MRCI levels of theory. As seen from both Table II and Fig. 1, the ground state of IrH_2 is a $^2A_1$ state with $r_e = 1.54$ Å and $\theta_e = 92°$. We expect the bond length to increase by 0.005 Å if 4f functions are included. There are two low-lying nearly degenerate excited $^2B_1$ and $^2A_2$ states for IrH_2. Three quartet electronic states are clustered near 1–1.1 eV region while the $^2B_2$ state is 1.8 eV above the ground state. The sextet states are noticeably higher but below the D_e of H_2.

In general higher-order correlation effects in the MRCI tend to shrink the Ir–H bonds although the changes in bond angles of the bent states are rather small (1°–6°). The ground state r_e changes at the MRCI level by $-$ 0.04 Å compared to the CAS-MCSCF level.

As seen from Table II, energy separations of excited electronic states are more sensitive to higher-order correlation effects. Among the doublet states, the $^2A_1$ ground state is more stabilized and thus the energy separations of the $^2B_1$ and $^2A_2$ states are much higher. The CASSCF and MRCI separations of the quartet states relative to the bent $^2A_1$ state are however, very comparable. The sextet states are more stabilized relative to the $^2A_1$ ground state at the MRCI level.

The bond lengths of the high spin states (quartet, sextet) are noticeably longer than the low spin doublet states. This is anticipated since the low spin states can form more

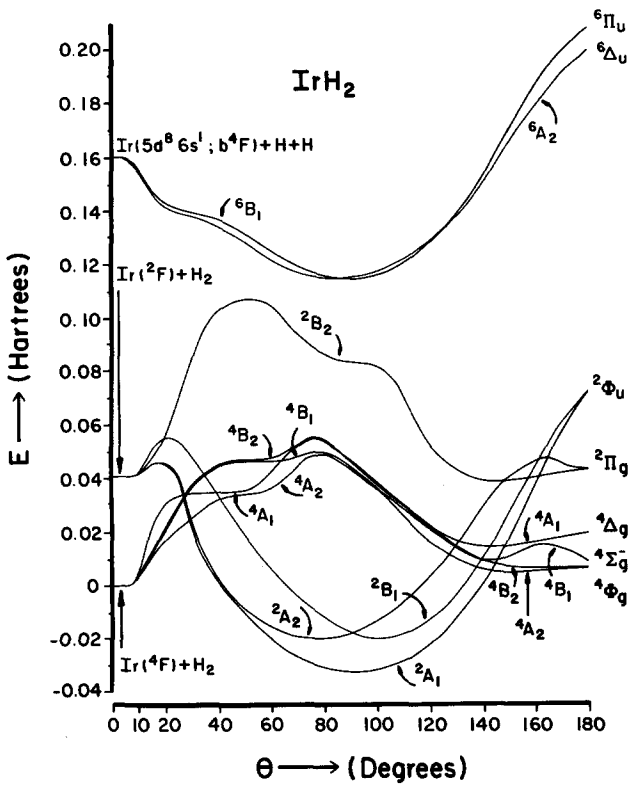

FIG. 1. Bending potential energy surfaces of 10 electronic states of IrH_2.

TABLE II. Properties of the bent electronic states of IrH_2 (without spin–orbit effect).

State	CASSCF θ_e, deg	CASSCF R_e, Å	CASSCF E, eV[a]	MRSDCI θ_e, deg	MRSDCI R_e, Å	MRSDCI E, eV[b]
$^2A_1$	91.8	1.575	0.00	91.9	1.540	0.00
$^2B_1$	102.2	1.578	0.34	105.6	1.548	0.65
$^2A_2$	75.9	1.568	0.34	74.5	1.541	0.68
$^4A_2$	148.0	1.684	1.04	142.5	1.640	1.02
$^4B_1$	143.5	1.689	1.25	137.7	1.658	1.12
$^4A_1$	144.4	1.694	1.26	139.7	1.656	1.13
$^2B_2$	145.9	1.673	1.92	141.7	1.631	1.80
$^6A_2$	84.4	1.737	3.99	81.8	1.728	3.87
$^6B_1$	88.3	1.728	3.99	88.2	1.722	3.95

[a] The zero CASSCF energy is for the $^2A_1$ bent minimum, and is $-105.056\,63$ hartree.

[b] The zero MRSDCI energy is for the $^2A_1$ bent minimum, and is $-105.175\,03$ hartree.

stable bond pairs with the H atoms compared to the high spin states which are relatively less bound.

As seen from Fig. 1, the Ir (^4F) ground state does not insert into H_2 spontaneously while the excited ^2F state inserts into H_2 spontaneously to form three stable doublet states namely, $^2A_1$, $^2A_2$ and $^2B_1$. The barriers in the quartet states are about 29 kcal/mol for insertion into H_2. However, the saddle points occur after the crossing of the quartet and doublet states. The lowest ($^4A_2$) surface crosses the $^2A_1$ state at ~ 11 kcal/mol above the Ir (^4F) + H_2 limit. Although the bond lengths at the crossing point are different, because of the large spin–orbit coupling of Ir which we discuss later, the quartet–doublet spin–orbit coupling matrix elements near the crossing are substantial enough to induce transition from the quartet surface to the doublet surface at sufficiently high relative velocities of collisions. Consequently, we estimate that the Ir (^4F) ground state atom has to surmount a much smaller barrier of 10–15 kcal/mol for insertion into H_2 since the nonadiabatic transition probability for the quartet–doublet transition is nonnegligible. This is indeed a much smaller barrier for a high spin ground state compared to any first and second row transition metal atoms.

All quartet states of IrH_2 correlate into two E states in the C_{2v}^2 double group. The $^2A_1$ state gives rise to an E state. For example, the $^2A_1$ state with α spin can mix with $^4A_2$ with appropriate spin combinations. Similarly, the $^2A_2$ state with α spin can mix with $^4A_1$ state with the spin combinations $\alpha\beta\alpha$, $\alpha\alpha\beta$, $\beta\alpha\alpha$ and $\beta\beta\beta$. Note that the $^4A_1$–$^2A_2$ crossing is very close to the $^4A_1$–$^2A_1$ crossing. In the next section, we describe the spin–orbit matrix elements coupling these states. Hence Ir + H_2 PES are very interesting from the standpoint of spin–orbit induced enhancement of reactivity with H_2.

There are two sets of sextet surfaces for IrH_2. The electronic states which correlate into Ir (^6D) + H_2 are only roughly ~ 5000 cm^{-1} above the sextet surfaces studied here at the dissociation limit. This ^6D state arises from the $5d^7 6s6p$ configuration of Ir.[32] However, we expect the sextet surfaces from Ir (^6D) + H_2 to have large barriers for insertion into H_2. The sextet states correlating into Ir ($b\,^4F$) + H(^2s) + H(^2s) exhibit bent minima in the PES of $^6B_1$ and $^6A_2$ states in Fig. 1. Therefore the sextet minima of IrH_2 with θ_e close to the θ_e of the $^2A_1$ ground state would provide channels for photoinduced dissociation of H_2 into H + H if excitation to the sextet states can be accomplished.

TABLE III. Properties of the linear electronic states of IrH_2 (without spin–orbit effect).[a]

Leading configuration	State	CASSCF R_e, Å	CASSCF E, eV	MRSDCI R_e, Å	MRSDCI E, eV
$1\sigma_g^2 2\sigma_g^1 \sigma_u^2 \delta_g^3 \pi_g^3$	$^4\Phi_g$	1.719	1.07	1.694	1.29
$1\sigma_g^2 2\sigma_g^1 \sigma_u^2 \delta_g^2 \pi_g^4$	$^4\Sigma_g^-$	1.711	1.12	1.685	1.28
$1\sigma_g^2 2\sigma_g^2 \sigma_u^2 \delta_g^3 \pi_g^2$	$^4\Delta_g$	1.737	1.43	1.711	1.43
$\sigma_g^2 \sigma_u^2 \delta_g^4 \pi_g^3$	$^2\Pi_g$	1.711	2.06	1.684	2.17
$1\sigma_g^2 2\sigma_g^2 \sigma_u \delta_g^3 \pi_g^3$	$^2\Phi_u$	1.770	2.84	1.713	2.91
$1\sigma_g^1 2\sigma_g^1 \sigma_u^2 \delta_g^1 \pi_g^2 \pi_u^3$	$^6\Delta_u$	1.678	6.35	1.639	7.40
$1\sigma_g^1 2\sigma_g^1 \sigma_u^2 \pi_g^2 \pi_u^4 2\pi_u^1$	$^6\Pi_u$	1.694	6.58	1.686	7.56

[a] All energies relative to the bent $^2A_1$ minimum.

Table III shows the geometries and energy separations of linear states of IrH_2. In general linear stationary points form longer Ir–H bonds since the Ir–H overlaps are considerably smaller for linear geometries. A primary reason for this is that in the linear states, the Ir ($d\delta_{x^2-z^2}$) orbital cannot participate in bonding. The primary overlap in the σ_g orbitals of linear states is through the Ir ($5d\sigma$) + H($1s$) and Ir ($6s$) + H($1s$) interactions.

The linear electronic states are in general above the corresponding bent states with the exception of the $^2B_2$ state for which the $^2B_2$–$^2\Pi_g$ energy separation is small as this state forms an obtuse angle minimum primarily through the Ir $d^7s^2 + d^7sp$ mixing.

The $^2B_2$ bending PES has a shoulder after the saddle point. This shoulder arises from an avoided crossing. The saddle points in some of the quartet states arise from several avoided crossings discussed in Sec. IV A 1.

2. Spin–orbit effects for IrH_2

Table IV shows the effect of spin–orbit (SO) coupling on the low-lying doublet state of IrH_2 near their minima. As

TABLE IV. Properties of the bent states of IrH_2 including spin–orbit effect.

State	θ_e, deg SO	θ_e, deg No SO	R_e, Å SO	R_e, Å No SO	E, eV[a] SO	E, eV[a] No SO
E(I) ($^2A_1$)	91.5	91.9	1.545	1.540	0.00	0.00
E(II) ($^2A_2$)	78.1	74.5	1.541	1.541	1.26	0.68
E(III) ($^2B_1$)	96.1	105.6	1.547	1.548	1.33	0.65

[a] The zero MRSDCI energy including spin–orbit effect is for the E(I) ($^2A_1$) bent minimum.

seen from Table IV, the geometry of the $E(I)$ state which is predominantly $^2A_1$, changes a bit due to spin–orbit coupling although it is stabilized to a significant extent. The most dramatic change in the H–Ir–H bond angle is seen in the E(III) state which is predominantly $^2B_1$. The θ_e of this state is significantly reduced ($\sim$9.5°).

As seen from Fig. 1, the $^2A_2$ and $^2B_1$ states cross. In the C_{2v}^2 double group both states give rise to E states. That is, in the presence of SO coupling, the $^2A_2$ state with the open shell spin α undergoes significant spin–orbit mixing with the $^2B_2$ state with open shell spin β, since

$$\langle a_1\alpha|H^{so}|b_1\beta\rangle \neq 0,$$
$$\langle a_1\alpha|H^{so}|b_2\beta\rangle \neq 0,$$
$$\langle a_1\alpha|H^{so}|a_2\alpha\rangle \neq 0.$$

Near the crossing regions these two states therefore undergo avoided crossing when SO coupling is included. Since the $^2B_1$ state has a large bond angle while the $^2A_2$ state has a much smaller bond angle, the θ_e of the E(II) state is increased due to this spin–orbit contamination while the θ_e of the E(III) state is decreased significantly ($\sim$9.5°) due to SO coupling. Consequently, these states of IrH_2 present very interesting examples for which SO coupling makes a dramatic impact on bond angles. The only other case documented up to now is the $^3B_1$ (A_1) state of PbH_2[26] for which θ_e changes significantly due to the $^3B_1$ (A_1)–$^1A_1$ (A_1) spin–orbit mixing. The $^2B_2$ state does not make much contribution to any of the low-lying doublet states since this state is significantly higher in energy.

As seen from Table IV, when spin–orbit effects are included energy separations are almost doubled compared to the $^2A_1$–$^2A_2$ separation in the absence of spin–orbit effects. This is primarily a result of spin–orbit stabilization of the $^2A_1$ state due to contamination of $^2A_1$ with $^2A_2$ and $^2B_1$ states.

The crossings of the quartet surfaces of IrH_2 arising from Ir (^4F) + H_2 with the doublet surfaces, especially $^2A_1$, are very interesting from the standpoint of SO coupling (see Fig. 1). If the SO coupling between the quartet and doublet states is sufficiently large, indeed the transition probability for a transition from quartet to doublet surfaces will be sufficiently large to enhance the reactivity of the Ir (^4F) state with a much smaller barrier.

Table V shows the magnitude of the spin–orbit coupling matrix elements of the lowest $^2A_1$ state with various quartet states near the curve crossing (theta) obtained from our relativistic CI matrix. As seen from Table V, the spin–orbit coupling of the $^2A_1$ state with especially the $^4B_1$ state is very large as a typical matrix element between two primitive slater determinants is of the order of 0.010 88 hartrees. While some of this coupling will contribute to the $^2B_1$ state which is obtained only with a sign change of the spin functions, the final RCI wave function reveals that the $^2A_1$–$^4B_1$ coupling is nonnegligible. The primary state contributing to the facilitation of the Ir (^4F) insertion into H_2 is the $^4B_1$ state as seen from Table V. The $^4A_2$ state couples only to a small but nonnegligible extent. The transition probability can be significant enough that a measurable number of quartet→doublet surface hoppings occur to enhance the reactivity of Ir (^4F). Consequently, due to the nonnegligible spin–orbit coupling between $^2A_1$ and $^4B_1$, we conclude that Ir (^4F) will insert into H_2 through transitions facilitated by the spin–orbit coupling.

The analysis of the relativistic CI calculations which included both doublet and quartet states at the curve crossing revealed that the contribution to the $^2A_1$ state near crossing by $^4B_1$ is 1.5%, while $^4B_2$ and $^4A_2$ states made only 0.3% and 0.05% contribution, respectively, near the curve crossings. This is fully consistent with the spin–orbit matrix elements coupling these states.

3. Dissociation energies

Table VI shows the dissociation energies of the low-lying states of IrH_2 with respect to Ir (^4F) + H_2 in the absence of spin–orbit effects. In general MRCI calculations stabilize the ground state much more compared to CASSCF calculations. The $^2A_1$ ground state of IrH_2 is 28 kcal/mol more stable than Ir (^4F) + H_2 in the absence of spin–orbit effects. However, as noted above spin–orbit effects are significant for IrH_2. The Ir (^4F) atomic state is stabilized by 10.4 kcal/mol due to spin–orbit coupling. The $E(I)$ state is stabilized

TABLE V. The magnitudes of the spin–orbit matrix elements for IrH_2 and IrH_2^+ at the doublet–quartet and triplet–quintet crossings, respectively.

			IrH_2		
		$^4A_2$ ($\alpha\alpha\beta$)	$^4A_2$ ($\alpha\beta\alpha$)	$^4B_1$ ($\beta\beta\alpha$)	$^4B_1$ ($\alpha\beta\beta$)
$^2A_1\alpha$		0.000 47	0.000 47	0.010 88	0.010 88
			IrH_2^+		
	$^5B_2$ ($\alpha\alpha\alpha\beta$)	$^5B_2$ ($\alpha\beta\beta\beta$)	$^5A_2$ ($\alpha\alpha\beta\beta$)	$^5B_1$($\alpha\alpha\alpha\beta$)	$^5B_1$($\alpha\beta\beta\beta$)
$^3A_2$ ($\alpha\beta$)	0.003 497	0.003 497	0.000 049	0.003 56	0.003 56
	$^5B_2$ ($\beta\alpha\alpha\alpha$)	$^5B_2$ ($\beta\beta\beta\alpha$)	$^5A_2$ ($\beta\beta\alpha\alpha$)	$^5B_1$($\beta\alpha\alpha\alpha$)	$^5B_1$($\beta\beta\beta\alpha$)
$^3A_2$ ($\beta\alpha$)	0.003 497	0.003 497	0.000 49	0.003 56	0.003 56

[a] Units are in hartrees. The spin combination shows the spin functions in the order of open shell orbitals in that Slater determinant. Only nonzero matrix elements are shown.

TABLE VI. Dissociation energies (Ir–H_2) of IrH_2 with respect to Ir (^4F) + H_2 (without spin–orbit effect).

State	CASSCF (kcal/mol)	MRSDCI (kcal/mol)
$^2A_1$	21	28
$^2B_1$	13	13
$^2A_2$	13	12
$^4A_2$	−4	5
$^4B_1$	−8	2
$^4A_1$	−9	2
$^2B_2$	−24	−13

by 9.8 kcal/mol. Therefore, the effective stability of the $E(I)$ state of IrH_2 with respect to the lowest Ir ($^4F_{9/2}$) + H_2 is 27.4 kcal/mol. The stability of this state with respect to the Ir ($^2F_{5/2}$) state is considerably higher. Based on the atomic $^4F_{9/2}$–$^2F_{5/2}$ separation of 10 579 cm^{-1},[32] we estimate that the dissociation energy of the $E(I)$ state of IrH_2 with respect to Ir ($^2F_{5/2}$) + H_2 is 57.6 kcal/mol. Consequently, both with respect to Ir ($^4F_{9/2}$) and Ir ($^2F_{5/2}$), the $E(I)$ ground state of IrH_2 is very stable. For a product to have long enough life times to be seen in the supersonic beam it should be at least 19 kcal/mol more stable than the dissociated M + H_2. Since IrH_2 is ~27 kcal/mol more stable than Ir ($^4F_{9/2}$) + H_2, it should definitely be a very stable molecule and detectable in a supersonic beam. Up to now the isolated IrH_2 molecule has not been experimentally characterized, although as noted in the introduction IrH_2 is characterized as a subunit in larger organometallic complexes. We hope that this study will stimulate such experimental investigations of IrH_2.

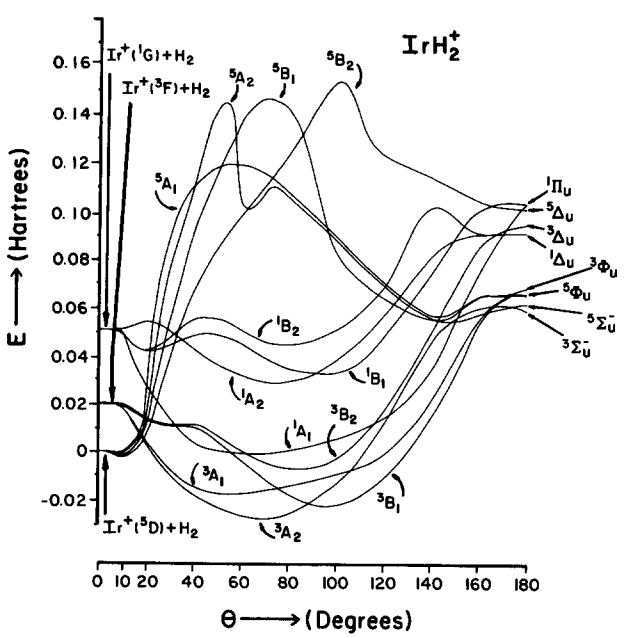

FIG. 2. Bending PES of 12 electronic states of IrH_2^+.

TABLE VII. Properties of bent electronic states of IrH_2^+ (without spin–orbit effect).

	CASSCF			MRSDCI		
State	θ_e, deg	R_e, Å	E, eV[a]	θ_e, deg	R_e, Å	E eV[b]
$^3A_2$	69.8	1.573	0.00	70.2	1.551	0.00
$^3B_1$	96.9	1.582	0.14	92.4	1.552	0.04
$^3A_1$	57.3	1.582	0.29	53.6	1.554	0.19
$^3B_2$	82.3	1.604	0.57	82.0	1.566	0.55
$^1A_1$	60.4	1.570	0.73	59.0	1.538	0.66
$^1A_2$	74.8	1.572	1.52	73.5	1.540	1.34
$^1B_1$	92.2	1.579	1.62	92.2	1.544	1.45
$^1B_2$	80.9	1.598	1.98	81.2	1.565	1.78
$^5B_1$	142.9	1.684	2.24	141.2	1.651	2.00
$^5A_2$	148.1	1.678	2.24	145.0	1.635	2.00
$^5A_1$	144.4	1.685	2.27	142.5	1.652	2.03

[a] The zero CASSCF energy is for the $^3A_2$ bent minimum and is −104.793 41 hartree.

[b] The zero MRSDCI energy is for the $^3A_2$ bent minimum and is −104.877 69 hartree.

C. IrH_2^+

1. Potential energy surfaces of IrH_2^+

Figure 2 shows the bending potential energy surfaces of the IrH_2^+ positive ion. Experimental information on Ir^+ is not available as Moore's Table[32] contains no information on the ground state or excited states of Ir^+. However, based on the well characterized, energy separations of the isoelectronic Os atom,[32] we believe that our predicted ground state of Ir^+ as well as the energy separations of the excited states are reasonable. Since we did not study the heptet states of IrH_2^+, the possibility of a heptet ground state of Ir^+ cannot be ruled out, but it is evident that the heptet states will not form low-lying minima. Nor will the heptet state insert into H_2 spontaneously.

As seen from Fig. 2, the low-lying Ir^+ (^3F) state inserts into H_2 spontaneously while the Ir^+ (^5D) state has to surmount a large barrier by itself to insert into H_2. However, as we discuss later the spin–orbit coupling plays a key role in changing the course of reactivity of Ir^+ (^5D) state through spin–orbit coupling of the triplet and quintet states of IrH_2^+.

The insertion of Ir^+ (^3F) into H_2 leads to at least four bent minima of $^3A_2$, $^3B_1$, $^3A_1$ and $^3A_2$ symmetries. Table VII shows the geometries and energy separations of the bent electronic states of IrH_2^+. As seen from Table VII, the $^3A_2$ and $^3B_1$ electronic states of IrH_2^+ are nearly degenerate. At the MRCI level $^3A_2$–$^3B_1$ energy separation is only 0.9 kcal/mol. As seen from Fig. 2, at the lower CAS-MCSCF level this separation is a bit larger. The $^3A_2$ forms a minimum at $\theta_e = 70.2°$ and $r_e = 1.551$ Å. The $^3B_1$ minimum has a much larger bond angle of 92°. The bond lengths of all triplet minima are quite comparable. With the exception of the $^3B_2$ state of IrH_2^+, all other triplet states become closer to the $^3A_2$ ground state at the higher MRCI level. This suggests that the $^3A_2$ state of IrH_2^+ is slightly destabilized relative to $^3B_1$ and $^3A_1$ states due to higher-order correlation effects.

The singlet states of IrH_2^+ arise from the insertion of Ir^+ (^1G) into H_2. Note that our assignment of the singlet dissociation into Ir^+ (^1G) is tentative but based on the known experimental data on Os.[32] As seen from Fig. 2, the insertion of Ir^+ (^1G) into H_2 is spontaneous. Among various singlet states thus formed, the $^1A_1$ state is especially more stable. At the final MRCI level, the $^1A_1$ state is 0.66 eV above the $^3A_2$ state. The $^1A_1$ state forms a minimum near 60° but the bending surface is somewhat shallow for this state. All other singlet states form bent minima with $\theta_e = 73°$–92°. The energy separations of these states are also significantly higher.

In comparing the $^2A_1$ ground state of IrH_2 with the two lowest states of IrH_2^+, we find that $\Delta\theta_e$ for the $^3B_1$ state is almost zero. Similarly Δr_e is only + 0.012 Å. This means that the Franck–Condon factor for the IrH_2 ($^2A_1$) → IrH_2^+ ($^3B_1$) transition will be large and thus the photoelectron spectrum corresponding to this transition will show a very narrow and sharp peak without much vibrational structure.

The IrH_2 ($^2A_1$) → IrH_2^+ ($^3A_2$) transition involves a large bond angle change ($\Delta\theta_e = -22°$) and somewhat smaller r_e changes. Consequently, this transition would have a smaller Franck–Condon factor and the spectral peak will be broad for this transition.

As seen from Fig. 2, although the quintet surfaces have large barriers, they cross the triplet surfaces much closer to the dissociation limit. The sharp barriers in all quintet surfaces arise from avoided crossings which we discuss in Sec. IV B 1.

The $^5B_2$ surface crosses the $^3A_2$ and $^3A_1$ surfaces. Similarly, all of the quintet surfaces cross the $^3A_2$ and $^3A_1$ surfaces in this region. The energy barrier at the crossing is only 2.5 kcal/mol. The $^5B_2$ state correlates into B_1, B_2, $2A_1$, and A_2 states in the C_{2v}^2 double group. The $^3A_2$ state correlates into A_1, B_1 and B_2 states while the $^3A_1$ state correlates into A_2, B_1 and B_2. Consequently, the interaction of the spin–orbit state of a given symmetry arising from the quintet states with the corresponding spin–orbit state arising from $^3A_1$ and $^3A_2$ could be significant. The spin–orbit coupling near the crossing regions are discussed in the next subsection. The nonadiabatic transition probability for the quintet surfaces to hop to triplet states through significant spin–orbit contamination in the region of curve crossings is found to be nonnegligible. Since the energy barrier at the crossing region is only 2.5 kcal/mol, the probability of Ir^+ in its ground state inserting into H_2 is nonzero. Spin–orbit effect therefore seems to be the most important effect in governing the reactivity of Ir and Ir^+ towards H_2.

The crossing of $^3A_2$ and $^3B_1$ surfaces, $^3A_1$ and $^3B_1$ surfaces and $^1A_1$ and $^3B_1$ surfaces, etc., seen in Fig. 2 induce significant spin–orbit contaminations among states of the same symmetry in the presence of spin–orbit coupling. Crossing of $^1B_1$ with $^1A_2$ will, however, not induce any spin–orbit coupling among these states since $^1B_1$ correlates into B_1 while $^1A_2$ correlates into the A_2 state when spin–orbit effects are included.

Table VIII shows the energy separations of linear electronic states of IrH_2^+. A critical comparison of the Ir–H bond lengths of the linear and bent states reveals that in general, linear states form significantly longer Ir–H bonds compared to the bent states. This is consistent with the corresponding bond lengths of linear states of IrH_2. In general, linear states are destabilized relative to the bent states at the higher MRCI level of theory. It is quite interesting that high spin states form more stable linear minima while for the low spin triplet and singlet states the linear stationary points are saddle points as evidenced from Fig. 2.

TABLE VIII. Properties of the linear electronic states of IrH_2^+ (without spin–orbit effect).[a]

Leading configuration	State	CASSCF R_e, Å	CASSCF E, eV	MRSDCI R_e, Å	MRSDCI E, eV
$1\sigma_g^2 2\sigma_g^1 \sigma_u^1 \delta_g^2 \pi_g^4$	$^3\Sigma_u^-$	1.748	2.35	1.712	2.57
$1\sigma_g^2 2\sigma_g^1 \sigma_u^1 \delta_g^2 \pi_g^4$	$^5\Sigma_u^-$	1.741	2.41	1.692	2.50
$1\sigma_g^2 2\sigma_g^1 \sigma_u^1 \delta_g^3 \pi_g^3$	$^5\Phi_u$	1.763	2.55	1.718	2.67
$1\sigma_g^2 2\sigma_g^1 \sigma_u^1 \delta_g^3 \pi_g^3$	$^3\Phi_u$	1.813	2.60	1.755	2.92
$\sigma_g^2 \sigma_u^1 \delta_g^3 \pi_g^4$	$^1\Delta_u$	1.740	3.23	1.687	3.25
$\sigma_g^2 \sigma_u^1 \delta_g^3 \pi_g^4$	$^3\Delta_u$	1.736	3.34	1.691	3.37
$1\sigma_g^2 2\sigma_g^2 \sigma_u^1 \delta_g^3 \pi_g^2$	$^5\Delta_u$	1.839	3.50	1.800	3.55
$\sigma_g^2 \sigma_u^1 \delta_g^4 \pi_g^3$	$^1\Pi_u$	1.797	3.52	1.742	3.67

[a] All energies relative to the $^3A_2$ bent minimum.

2. Spin–orbit effects for IrH_2^+

Table IX shows the effect of spin–orbit coupling on the low-lying triplet states of IrH_2^+ near their minima. As seen from Table IX the spin–orbit effects are very significant for IrH_2^+. All the spin–orbit components of the $^3A_2$ state are stabilized relative to the $^3A_2$ state.

The change in the H–Ir–H bond angle of the $^3A_2$ (A_1) component is dramatic (~9.3°) mainly due to the strong mixing of $^3A_2$ (A_1) with $^3B_2$ (A_1) as well as $^3B_1$ (A_1) and $^1A_1$ (A_1) states. Since the nearly degenerate $^3B_1$ state has a much larger θ_e of 92.4°, the strong mixing of $^3B_1$ (A_1) with

TABLE IX. Properties of the bent states of IrH_2^+ including spin–orbit effect.

State	θ_e, deg	R_e, Å	E, eV
$^3A_2$ (A_1)	79.5	1.557	0.00
$^3A_2$ (B_1)	72.8	1.556	0.19
$^3A_2$ (B_2)	71.4	1.552	0.27
$^3A_2$	70.2	1.551	0.38
$^3B_1$ (A_1)	83.6	1.548	0.34
$^3B_1$ (B_2)	85.6	1.550	0.39
$^3B_1$ (A_2)	89.6	1.545	0.39
$^3B_1$	92.4	1.552	0.42
$^3B_2$ (A_2)	83.1	1.566	0.88
$^3B_2$ (B_1)	82.1	1.560	1.01
$^3B_2$ (A_1)	81.1	1.560	1.09
$^3B_2$	82.0	1.566	0.93

$^3A_2$ (A_1) changes the θ_es of the corresponding components significantly. Note that the θ_e of the $^3B_1$ (A_1) decreases by 9° while the θ_e of the $^3A_2$ (A_1) states increases by almost the same amount. The other spin–orbit components are less influenced.

The energy separations are sensitive to the inclusion of spin–orbit coupling as expected for IrH_2^+. As seen from Table IX the $^3A_2$ (A_1)–$^3A_2$ (B_2) energy separation is 0.27 eV while these states are degenerate in the absence of SO coupling.

Table V shows the spin–orbit matrix elements between the two primitive determinants of the $^3A_2$ states of IrH_2^+ with various quintet states near the region of quintet–triplet curve crossings at small bond angles (Fig. 2). As discussed before for IrH_2, the transition probability for $Ir^+ + H_2$ collision to hop from a quintet to triplet surface will depend on the spin–orbit coupling matrix element since the energy separation at the curve crossing is related to the spin–orbit matrix elements.

As seen from Table V, the SO coupling between the $^3A_2$ state with determinants that give rise to $^5B_2$ and $^5B_1$ are significant (total of eight matrix elements each = 0.0035 hartrees). Consequently, the quintet–triplet SO coupling for IrH_2^+ is quite comparable to the quartet–doublet SO coupling for IrH_2 at similar curve crossings.

The analysis of the final RCI wave function at curve crossing region reveals that the $^3A_2$ (A_1) state is composed of 69% $^3A_2$, 15% $^3B_2$, 11% $^3B_1$, 1.5% $^5B_2$ and 1.3% $^5B_1$. Hence the total quintet contamination to the $^3A_2$ (A_1) state is 2.8% through primary configurations and up to 1% through secondary excited quintet configurations. Similar composition was found for other spin–orbit states arising from the triplet states.

The above analyses of RCI wave functions and SO coupling matrix in the curve-crossing region reveal that the nonadiabatic transition probability for the quintet surfaces to hop to the triplet states is nonnegligible. This contrasts with the higher second and first row MH_2 species for which the spin–orbit contamination of different spin multiplets are smaller. Therefore we conclude that a nonzero number of nonadiabatic quintet–triplet transitions will occur in the curve-crossing regions thereby facilitating spin–orbit enhanced reactivity of the quintet state of Ir^+.

3. Adiabatic ionization potential of IrH_2

The adiabatic IP of IrH_2 was obtained both with and without SO effects. At the lower CAS-MCSCF level of theory the IP is only 7.2 eV while at the superior MRCI level of theory the adiabatic IP of IrH_2^+ is 8.1 eV. Since the spin–orbit effects of IrH_2 and IrH_2^+ are comparable, the net result of this effect is to increase the IP by 0.1 eV. The final IP of IrH_2 including SO coupling is calculated as 8.2 eV. The CAS-MCSCF level of theory underestimates the IP by almost 0.9 eV. This is not surprising in view of the large electron correlation effects for IrH_2. Since the adiabatic IP of IrH_2 has been determined, the photoelectron spectra of IrH_2 can be predicted using the energy separations of electronic states of IrH_2 and IrH_2^+. We note that our final SO corrected MRCI IP of 8.2 eV is likely to be smaller than the true value since our calculations underestimate the IP of the Ir atom by 0.4 eV compared to the experimental value.

TABLE X. Dissociation energies of IrH_2^+ without spin–orbit effect.[a]

State	CASSCF (kcal/mol)	MRSDCI (kcal/mol)
$^3A_2$	17	30
$^3B_1$	14	29
$^3A_1$	11	25
$^3B_2$	4	17
$^1A_1$	0	14
$^1A_2$	−18	1
$^1B_1$	−20	−4
$^1B_2$	−28	−11
$^5A_2$	−34	−16
$^5B_1$	−34	−16
$^5A_1$	−35	−17

[a]With respect to Ir^+ (^5D) + H_2.

4. Dissociation energies of IrH_2^+

Table X shows the dissociation energies of IrH_2^+ in the absence of spin–orbit effects with respect to Ir^+ (^5D) + H_2 dissociation limit. As seen from Table X, the IrH_2^+ $^3A_2$ ground state is 30 kcal/mol more stable than Ir (^5D) + H_2. When compared to the dissociation energy of IrH_2 we find that IrH_2^+ is 2 kcal/mol more stable compared to IrH_2 for dissociation in the absence of SO coupling. As evidenced from Table X, the MRCI calculations increase the D_e of IrH_2^+ by almost 13 kcal/mol indicating that electron correlation effects have significant effect especially on binding energies.

Although the higher singlet states of IrH_2^+ are not bound with respect to Ir^+ (^5D) + H_2, they are bound with respect to their own singlet dissociation limits, viz., Ir^+ (^1G) + H_2. For such a heavy ion however, the crossing of quintet surfaces with these singlet surfaces in Fig. 2, would lead to predissociation into Ir^+ (^5D) + H_2. Consequently, all D_e's are listed with respect to Ir^+ (^5D) + H_2.

Next we consider the effect of spin–orbit coupling on the D_e. The $^3A_2$ (A_1) state of IrH_2^+ in the C_{2v}^2 double group is stabilized by 0.38 eV due to spin–orbit coupling. The Ir^+ ($^5D_4$) state is stabilized by ~0.3 eV due to spin–orbit coupling. But the A_1 spin–orbit state dissociates into Ir^+ ($^5D_0$) + H_2 which is estimated at 0.7 eV above the $^5D_4$ state based on the electronic states of Os. Consequently, the D_e of the A_1 spin–orbit state of IrH_2^+ with respect to Ir^+ ($^5D_0$) + H_2 is estimated as to be 18 kcal/mol more than its value in the absence of SO coupling or 48 kcal/mol.

IV. THE NATURE OF ELECTRONIC STATES AND PES OF IrH_2 AND IrH_2^+

A. IrH_2

1. The CI compositions, the shapes of PES, and the origins of saddle points

Table XI shows the contributions of leading configurations to the MRSDCI wave function of IrH_2. While the

TABLE XI. Leading configurations in the MRSDCI of the bent states of IrH_2.

State	Coefficient	Configuration							
		$1a_1$	$2a_1$	$3a_1$	$4a_1$	$1b_2$	$2b_2$	$1b_1$	$1a_2$
$^2A_1$	0.951	2	2	1	0	2	0	2	2
$^2B_1$	−0.951	2	2	2	0	2	0	1	2
$^2A_2$	−0.953	2	2	2	0	2	0	2	1
$^4A_2$	−0.961	2	2	1	0	2	1	1	2
$^4B_1$	−0.959	2	2	1	0	2	1	2	1
$^4A_1$	0.959	2	2	2	0	2	1	1	1
$^2B_2$	0.579	2	2	0	0	2	1	2	2
	0.514	2	1	1	0	2	1	2	2
	−0.400	2	0	2	0	2	1	2	2
	−0.361	2	2	2	0	2	1	0	2
$^6A_2$	0.958	2	1	1	1	2	1	1	2
$^6B_1$	0.959	2	1	1	1	2	1	2	1

lowest $^2A_1$, $^2B_1$, $^2A_2$ and three quartet states are simple in composition this is not so for the $^2B_2$ state. This explains the shape of the PES of the $^2B_2$ state in Fig. 1. The obtuse θ_e in the $^2B_2$ state arises from avoided crossings of $1a_1^2 2a_1^2 1b_2^2 2b_2 1b_1^2 1a_2^2$ with $1a_1^2 2a_1 3a_1 1b_2^2 2b_2 1b_1^2 1a_2^2$, $1a_1^2 3a_1^2 1b_2^2 2b_2 1b_1^2 1a_2^2$, and $1a_1^2 2a_1^2 3a_1^2 1b_2^2 2b_2 1a_2^2$ configurations. The shoulder in the $^2B_2$ PES also is due to avoided crossings. All other bent electronic states of IrH_2 are well represented by a single configuration (Table XI).

At $\theta = 20°$ the $^2B_2$ state is 27% $1a_1^2 2a_1^2 3a_1 4a_1 1b_2 1b_1^2 1a_2^2$, 25% $1a_1^2 2a_1^2 3a_1^2 4a_1 1b_2^2 1b_1 1a_2$, 19% $1a_1^2 2a_1^2 3a_1^2 1b_2 1b_1^2 1a_2^2$, etc. At $\theta = 40°$ this state becomes 94% $1a_1^2 2a_1^2 3a_1^2 1b_2 1b_1^2 1a_2^2$. Consequently, the saddle point in this region of the $^2B_2$ state arises from this avoided crossing. At $\theta = 60°$, this state becomes 89% $1a_1^2 2a_1^2 3a_1 1b_2^2 2b_2 1b_1^2 1a_2^2$. This avoided crossing explains the shoulder in the $^2B_2$ PES beyond the saddle point. At $\theta = 80°$, this state is 63% $1a_1^2 2a_1 3a_1 1b_2^2 2b_2 1b_1^2 1a_2^2$ and 14% $1a_1^2 2a_1^2 1b_2^2 2b_2 1b_1^2 1a_2^2$ and 11% $1a_1^2 3a_1^2 1b_2^2 2b_2 1b_1^2 1a_2^2$. This explains the second shoulder. The composition of the $^2B_2$ state is quite complex near its obtuse θ_e as seen from Table XI.

The $^4A_2$ state at $\theta = 20°$ is composed of 98% $1a_1^2 2a_1^2 3a_1 4a_1 1b_2^2 1b_1^2 1a_2$. At $\theta = 80°$, it is still dominated by this configuration. Consequently, the broad saddle points in the $^4A_2$ and other quartet states are natural barriers and arise from changes in the antibonding orbital interactions to bonding interactions while the saddle point in the $^2B_2$ state at very acute θ occurs due to avoided crossings discussed above.

Among the linear electronic states of IrH_2, the $^4\Delta_g$, $^4\Phi_g$, $^6\Delta_u$, $^6\Pi_u$, $^2\Phi_u$ states are well represented by one or two configurations. But the $^4\Sigma_g^-$ and $^2\Pi_g$ states need a multiconfigurational treatment. The mixing of the $\sigma_g\delta_g^2$ and $\sigma_g\pi_g^2$ configurations in the $^4\Sigma_g^-$ state are very noticeable (Table XII).

2. Dipole moments

Table XIII shows the dipole moments (μ_e) of the low-lying states of IrH_2. All μ_e in Table XIII have Ir^+H^- polarity. The large $\mu_e s$ of IrH_2 indicate the strong ionicities of the IrH bonds. The $\mu_e s$ of $^6A_2$ and $^6B_1$ states are significantly smaller as expected since these are high spin states. For the high spin states, the electron transfer from Ir to H is expected to be significantly smaller and thus the dipole moment is small for $^6A_2$ and $^6B_1$.

The $^2A_1$ and $^2A_2$ states have significantly larger $\mu_e s$ compared to $^2B_1$. As seen from Table II, the $\theta_e s$ of the $^2A_2$ and $^2A_1$ states are much smaller than the θ_e of the $^2B_1$ state. In general, as the bond angle is reduced, μ_e should become larger. For this reason the μ_e of the $^2B_2$ state is only 0.985 D since its $\theta_e \sim 142°$. The large $\mu_e s$ of the $^2A_1$ and $^2B_2$ states of IrH_2 are consistent with the electron rich character of Ir. The μ_e/r_e values for the $^2A_1$ and $^2A_2$ states are 1.42 and 1.44 D/Å, respectively.

The smaller dipole moments of the quartet states are consistent with both their high spin characters and the obtuse $\theta_e s$ of these states as seen from Table II.

TABLE XII. Important configurations in the MRSDCI of the linear states of IrH_2.[a]

State	Coefficient(s)	Configuration						
		$1\sigma_g$	$2\sigma_g$	σ_u	δ_g	π_g	$1\pi_u$	$2\pi_u$
$^4\Phi_g$	0.684, −0.684	2	1	2	3	3	0	0
$^4\Sigma_g^-$	0.849	2	1	2	2	4	0	0
	0.461	2	1	2	4	2	0	0
$^4\Delta_g$	−0.960	2	2	2	3	2	0	0
$^2\Phi_u$	0.596, −0.554, −0.367, 0.297	2	2	1	3	3	0	0
$^2\Pi_g$	−0.575	2	0	2	4	3	0	0
	−0.418, 0.400	2	1	2	3	3	0	0
	0.306, 0.297, −0.256	2	2	2	2	3	0	0
$^6\Delta_u$	0.981	1	1	2	1	3	3	0
$^6\Pi_u$	0.991	1	1	2	0	2	4	1

[a] Multiple CSFs for a given configuration have multiple coefficients in a line.

TABLE XIII. Dipole moment for the bent minimum of IrH_2.

State	μ, D[a]
$^2A_1$	2.18
$^2B_1$	1.79
$^2A_2$	2.22
$^4A_2$	1.09
$^4B_1$	1.25
$^4A_1$	1.20
$^2B_2$	0.99
$^6A_2$	0.61
$^6B_1$	0.47

[a]Polarity is Ir^+H^-.

3. Mulliken populations

Table XIV shows the Ir s, p, and d Mulliken populations of the electronic states of IrH_2. Due to the complexity of the Ir hybridization, Mulliken populations are by far one of the most useful quantities to gain insight into the nature of bonding in transition metal compounds although Mulliken populations are basis-set-dependent. As seen from Table XIV, in the ground state of IrH_2, Ir atom exhibits $5d^{8.1}6s^{0.75}6p^{0.12}$ hybridization. The remaining electron density from Ir is transferred to H atoms. This agrees reasonably with the fact that the Ir ($^2A_1$) state arises from the $5d^86s^1$ (^2F) configuration of the Ir atom. The $6p$ participation in the $^2A_1$ state is noticeable. In general, all doublet electronic states have considerably larger d populations compared to the quartet and sextet states.

The $^2B_1$ and $^2A_2$ electronic states of IrH_2 exhibit a more complex $5d^86s^1$, $5d^76s^2$ hybridization since their $6s$ Mulliken populations are larger while the d populations are smaller.

The $6p$ population in the quartet and sextet states are especially large. We are not surprised by the large $6p$ population in the $^6A_2$ and $^6B_1$ state since minima in these PES arise although correlating into Ir (^4F) + H (^2S) + H(^2S) there is a nearby Ir (^6D) state arising from the $5d^76s6p$ configuration.

In general, linear electronic states of a given spin multiplicity have enhanced $6p$ character compared to the bent states of the same spin multiplicity. This is in accord with the strong participation of the $6p$ orbital in the $1\sigma_u$ orbital in overlapping with H ($1s$) orbitals.

The Ir–H overlaps are significantly larger for the bent $^2A_1$, $^2B_1$ and $^2A_2$ states compared to the $^6A_2$ and $^6B_1$ (0.23–0.28) states. The Ir–H overlaps of these doublet states are also larger than the overlaps for the quartet states. This is consistent with the bond lengths of these states. The $^6A_2$ and $^6B_1$ states form a shallow minima. In general, high spin states have smaller overlaps and therefore longer bond lengths compared to the low-spin doublet states of IrH_2.

TABLE XIV. Mulliken population analyses for the electronic states of IrH_2.

State	Gross Ir (s)	Gross Ir (p)	Gross Ir (d)	Ir–H Overlaps
$^2A_1$	0.753	0.123	8.057	1.117
$^2B_1$	1.350	0.118	7.453	1.132
$^2A_2$	1.318	0.104	7.546	1.116
$^4A_2$	0.752	0.309	7.541	1.043
$^4B_1$	1.346	0.320	6.944	1.079
$^4A_1$	1.372	0.324	6.911	1.086
$^2B_2$	0.823	0.264	7.551	0.967
$^6A_2$	1.006	0.706	6.834	0.272
$^6B_1$	1.013	0.722	6.803	0.233
$^4\Phi_g$	0.857	0.384	7.289	1.096
$^4\Sigma_g^-$	0.892	0.392	7.263	1.088
$^4\Delta_g$	1.466	0.419	6.663	1.129
$^2\Pi_g$	0.861	0.378	7.295	1.079
$^2\Phi_u$	1.503	0.127	7.472	0.724

4. Relativistic CI compositions and spin–orbit mixings

Table XV shows the composition of RCI wave functions including spin–orbit coupling near the minima of three lowest states of IrH_2. We have already discussed the spin–orbit coupling matrix elements and the composition of RCI wave functions near quartet–doublet crossings. As seen from Table XV, the $^2A_1$ state in the absence of spin–orbit coupling becomes 63% $^2A_1$, 16% $^2B_1$ and 17% $^2A_2$. As seen from Fig. 1, near the well of the $^2A_1$ state of IrH_2, the $^2B_1$ and $^2A_2$ states cross and consequently, they make almost the same contribution. Hence the spin–orbit contamination is very large for IrH_2. Therefore we designate the lowest spin–orbit state as the E(I) state due to large spin–orbit contamination. The E(II) state which is predominantly $^2A_2$ is 65% $^2A_2$, 29% $^2A_1$ and only 2% $^2B_1$ near its minimum. The E(III) state is 65% $^2B_1$ and 29% $^2A_2$.

The large spin–orbit mixings discussed above not only change the energy separations of electronic states of IrH_2 significantly but also induce substantial changes in the bond angles (up to 9°) in the E (III) state. Note that the contribution of the $^2B_2$ state is negligible since this state is much higher in energy.

The large spin–orbit contamination of the three low-lying states will also have significant impact on the dipole moments of these states. Since the E(I) state is 63% $^2A_1$,

TABLE XV. The contributions of the various states in the RCI of IrH_2.

Relativistic state	Weights in percent
E(I) ($^2A_1$)	$1a_1^2 2a_1^2 3a_1^1 1b_2^2 1b_1^2 1a_2^2$ ($^2A_1$, 63%)
	$1a_1^2 2a_1^2 3a_1^2 1b_2^2 1b_1^1 1a_2^2$ ($^2B_1$, 16%)
	$1a_1^2 2a_1^2 3a_1^2 1b_2^2 1b_1^2 1a_2^1$ ($^2A_2$, 17%)
E (II) ($^2A_2$)	$1a_1^2 2a_1^2 3a_1^2 1b_2^2 1b_1^2 1a_2^1$ ($^2A_2$, 65%)
	$1a_1^2 2a_1^2 3a_1^1 1b_2^2 1b_1^2 1a_2^2$ ($^2A_1$, 29%)
	$1a_1^2 2a_1^2 3a_1^2 1b_2^2 1b_1^1 1a_2^2$ ($^2B_1$, 2%)
E(III) ($^2B_1$)	$1a_1^2 2a_1^2 3a_1^2 1b_2^2 1b_1^1 1a_2^2$ ($^2B_1$, 65%)
	$1a_1^2 2a_1^2 3a_1^2 1b_2^2 1b_1^2 1a_2^1$ ($^2A_2$, 29%)
	$1a_1^2 2a_1^2 3a_1^1 1b_2^2 1b_1^2 1a_2^2$ ($^2A_1$, 1%)

16% $^2B_1$, and 17% $^2A_2$ and since the μ_e of $^2B_1$ is significantly smaller, we estimate the μ_e of the ground state of IrH_2 to be reduced to 2.0 D based on a simple weighted average of the μ_es of the three doublet states as determined by the RCI composition. The dipole moment of the E(III) state to the contrary will increase.

B. IrH_2^+

1. The CI compositions and the nature of PES and the origins of saddle points in PES

Table XVI shows the leading configurations in the MRSDCI wave functions of bent electronic states of IrH_2^+. All four triplet states of IrH_2^+ are well described by a single leading configuration. With the exception of $^1A_1$ all other singlet states are well represented by their leading configurations. The $^1A_1$ state is, however, a mixture of $1a_1^2 2a_1^2 1b_2^2 1b_1^2 1a_2^2$, $1a_1^2 2a_1^2 3a_1^2 1b_2^2 1b_1^2$, and $1a_1^2 3a_1^2 1b_2^2 1b_1^2 1a_2^2$, configurations.

The saddle points in the $^5A_2$ state and $^5B_2$ state are somewhat narrow while the $^5A_1$ and $^5B_1$ states have relatively broad barriers. This contrast needs an explanation. Also the $^5A_2$ state has a sharp barrier followed by a minimum and another saddle point prior to the formation of a linear minimum (Fig. 2). These features in the $^5A_2$ PES are attributed to several avoided crossings.

The composition of the $^5A_2$ state at $\theta = 20°$ is 98% $1a_1^2 2a_1^2 3a_1 4a_1 1b_2 1b_1 1a_2^2$. At $\theta = 40°$ this state becomes 93% $1a_1^2 2a_1^2 3a_1 4a_1 1b_2 1b_1 1a_2^2$ and 5% $1a_1^2 2a_1 3a_1 1b_2 2b_2^2 1b_1 1a_2^2$. At $\theta = 60°$, the $^5A_2$ state becomes 93% $1a_1^2 2a_1 3a_1 4a_1 1b_2^2 1b_1^2 1a_2$ and 2% $1a_1^2 2a_1^2 3a_1 4a_1 1b_2 1b_1 1a_2^2$. Note that at this angle this state completely changes its composition. The avoided crossing between the $1a_1^2 2a_1 3a_1 4a_1 1b_2^2 1b_1^2 1a_2$ and $1a_1^2 2a_1^2 3a_1 4a_1 1b_2 1b_1 1a_2^2$ configurations of IrH_2^+ in the $^5A_2$ state lead to the narrow barrier followed by a minimum. At $\theta = 80°$, this state undergoes yet another avoided crossing since its composition changes to 93% $1a_1^2 2a_1 3a_1 1b_2^2 2b_2 1b_1 1a_2^2$. This configuration continues to dominate for $\theta > 100°$ also. Consequently, the double hump in the $^5A_2$ PES of IrH_2^+ is clearly a manifestation of these avoided crossings.

The $^5B_1$ state is predominantly $1a_1^2 2a_1^2 3a_1 4a_1 1b_2 1b_1^2 1a_2$ at $\theta = 20°$ and 40°. At $\theta = 60°$, however, it becomes 65% $1a_1^2 2a_1^2 3a_1 4a_1 1b_2 1b_1^2 1a_2$ and 17% $1a_1^2 2a_1 3a_1 1b_2^2 2b_2 1b_1^2 1a_2$. At $\theta = 80°$, this state changes to 55% $1a_1^2 2a_1 3a_1 1b_2^2 2b_2 1b_1^2 1a_2$ and 31% $1a_1^2 2a_1^2 3a_1 4a_1 1b_2 1b_1^2 1a_2$. The saddle point in the $^5B_1$ state therefore arises from this avoided crossing. At $\theta = 100°$ and larger angles the $1a_1^2 2a_1 3a_1 1b_2^2 2b_2 1b_1^2 1a_2$ configuration dominates in the $^5B_1$ state.

The $^5B_2$ state is predominantly $1a_1^2 2a_1^2 3a_1 4a_1 1b_2^2 1b_1 1a_2$ for $10° < \theta < 100°$. At $\theta = 120°$ it becomes 84% $1a_1^2 2a_1^2 3a_1^2 1b_2 2b_2 1b_1 1a_2$ and only 8% $1a_1^2 2a_1^2 3a_1 4a_1 1b_2^2 1b_1 1a_2$. Therefore the saddle point and the shape of the PES of the $^5B_2$ state is due to this avoided crossing since this occurs between $\theta = 100°$ and 120°. Note that the saddle point in this PES occurs in this region. At larger bond angles the $1a_1^2 2a_1^2 3a_1^2 1b_2 2b_2 1b_1 1a_2$ configuration dominates.

The $^5A_1$ state is dominated by the $1a_1^2 2a_1^2 3a_1^2 4a_1 1b_2 1b_1 1a_2$ configuration for $10° < \theta < 40°$. At $\theta = 60°$ this state becomes 89% $1a_1^2 2a_1^2 3a_1 1b_2^2 2b_2 1b_1 1a_2$ configuration. Consequently, the saddle point in this region is due to this avoided crossing. For larger bond angles the $1a_1^2 2a_1^2 3a_1 1b_2^2 2b_2 1b_1 1a_2$ configuration dominates.

The above analysis of the composition of the CI wave functions reveals that all saddle points in the quintet surfaces arise from avoided crossings. The general trend is that at small angles only the $1b_2$ orbital which is predominantly Ir (d) is occupied. At larger bond angles the occupancy of the $2b_2$ orbital becomes more significant as the overlap between Ir ($5d\pi$), Ir ($6p_y$) (smaller amount) and H_1 ($1s$)–H_2 ($1s$) orbital becomes larger as θ increases. This minimizes the antibonding interactions through favorable bonding interaction between Ir ($5d\pi$), Ir ($6p_y$), and H_2 ($1\sigma_u$) orbital. In those states for which this interaction occurs more readily, the dissociation of H_2 is facilitated. In general, low spin states readily rearrange to form strong Ir ($5d\pi$) + Ir($6p_y$) + H_2 ($1\sigma_u$) bonding interaction leading to the dissociation of H_2.

TABLE XVI. Leading configurations in the MRSDCI of the bent states of IrH_2^+.

State	Coefficient	Configuration							
		$1a_1$	$2a_1$	$3a_1$	$4a_1$	$1b_2$	$2b_2$	$1b_1$	$1a_2$
$^3A_2$	0.958	2	2	1	0	2	0	2	1
$^3B_1$	0.955	2	2	1	0	2	0	1	2
$^3A_1$	0.959	2	1	1	0	2	0	2	2
$^3B_2$	−0.956	2	2	2	0	2	0	1	1
$^1A_1$	−0.799	2	2	0	0	2	0	2	2
	0.414	2	2	2	0	2	0	2	0
	0.324	2	0	2	0	2	0	2	2
$^1A_2$	0.955	2	2	1	0	2	0	2	1
$^1B_1$	−0.955	2	2	1	0	2	0	1	2
$^1B_2$	−0.939	2	2	2	0	2	0	1	1
$^5B_1$	0.961	2	1	1	0	2	1	2	1
$^5A_2$	−0.955	2	1	1	0	2	1	1	2
$^5A_1$	0.963	2	2	1	0	2	1	1	1

2. Mulliken populations

Table XVII shows the Ir (6s, 6p and 5d) Mulliken populations and the total Ir–H overlap populations for various electronic state of IrH_2^+. As seen from Table XVII, in the $^3A_2$ ground state the Ir^+ exists in an effective configuration of Ir $6s^{0.62}6p^{0.12}5d^{7.5}$ as compared to the $^2A_1$ ground state of IrH_2 with an effective population of $6s^{0.75}6p^{0.12}5d^{8.1}$. Consequently, significant electronic density is lost by the 5d orbital upon ionization of IrH_2. The 6p population is nearly the same between neutral and the ionic species. The Ir–H overlaps of neutral and ionic species are also similar.

The quintet states have somewhat larger 6p populations compared to the triplet and singlet states. The $^1A_1$ state has a much smaller 6s population and a slightly larger 5d population. Therefore in the $^1A_1$ state the Ir^+ ion exhibits $5d^6 6s^1$ and $5d^7$ configurational mixing.

TABLE XVII. Mulliken population analyses for the electronic states of IrH_2^+.

State	Gross Ir (s)	Gross Ir (p)	Gross Ir (d)	Ir–H Overlaps
$^3A_2$	0.622	0.121	7.509	1.122
$^3B_1$	0.700	0.126	7.405	1.154
$^3A_1$	0.555	0.109	7.572	1.018
$^3B_2$	1.081	0.130	7.012	1.169
$^1A_1$	0.454	0.108	7.692	1.047
$^1A_2$	0.614	0.130	7.508	1.130
$^1B_1$	0.616	0.127	7.487	1.140
$^1B_2$	1.076	0.138	7.027	1.161
$^5B_1$	0.719	0.323	6.987	1.071
$^5A_2$	0.770	0.302	7.001	1.043
$^5A_1$	0.786	0.325	6.919	1.076

The sum of two Ir–H overlap populations of all states are > 1.0 indicating significant Ir–H bonding. This corroborates with shorter Ir–H bond lengths for the triplet and singlet states of IrH_2^+ but somewhat longer bond lengths for the quintet states. The quintet states have longer bond lengths since Ir^+ high spin state does not form strong bond pairs with H (1s) orbitals.

3. Composition of the relativistic CI wave functions and the effect of spin–orbit coupling

Table XVIII shows the weights of various configurations in the RCI wave functions of the electronic states of IrH_2^+. As seen from Table XVIII, various spin–orbit components of IrH_2^+ are heavily contaminated approaching an intermediate coupling. The $^3A_2$ (A_1) ground state of IrH_2^+ is 63% $^3A_2$, 15% $^3B_2$, 12% $^3B_1$ and 7% $^1A_1$. This large spin–orbit contamination increases the H–Ir–H bond angle of the ground state of IrH_2^+ by 9.3°. The increase in bond angle is consistent with the larger bond angle of the $^3B_1$ and $^3B_2$ states which are primary contaminators.

The $^3A_2$ (B_1) state cannot mix with $^3B_1$ since there is no spin–orbit state of the B_1 symmetry. Therefore the bond angle of the B_1 component changes by only 3°. The $^3A_2$ (B_2) component is contaminated by only 3% $^3B_1$ (B_2). The $^3B_1$ (B_2) is further high. Consequently, the bond angle of $^3A_2$ (B_2) changes by only 1°.

The $^3B_1$ (A_1) spin–orbit state is heavily mixed akin to the $^3A_2$ (A_1) state. Therefore the bond angle of $^3B_1$ (A_1) state reduces by ~9° relative to $^3B_1$ (NOSO) due to contamination with $^3A_2$. Therefore we conclude that spin–orbit contaminations of different states of IrH_2^+ are very significant.

TABLE XVIII. The contributions of the various states in the RCI of IrH_2^+.

Relativistic state	Weight in percent
$^3A_2(A_1)$	63% $^3A_2$, 15% $^3B_2$, 12% $^3B_1$, 7% $^1A_1$
$^3A_2(B_1)$	85% $^3A_2$, 14% $^3B_2$
$^3A_2(B_2)$	94% $^3A_2$, 2.5% $^3B_1$, 2.2% $^1B_2$
$^3B_1(A_1)$	60% $^3B_1$, 26% $^3A_2$, 11% $^1A_1$
$^3B_1(B_2)$	90% $^3B_1$, 5.3% $^1B_2$, 3.4% $^3A_2$
$^3B_1(A_2)$	96% $^3B_1$, 3% $^1A_2$
$^3B_2(A_2)$	96% $^3B_2$, 0.01% $^1A_2$, 0.01% $^3B_1$
$^3B_2(B_1)$	75% $^3B_2$, 14% $^3A_2$, 8.6% $^1B_1$
$^3B_2(A_1)$	79% $^3B_2$, 8.5% $^1A_1$, 7.9% $^3A_2$, 2.3% $^3B_1$

V. COMPARISON OF IrH_2 WITH RhH_2

In a previous study one of the authors and Liao[34] investigated the PES of RhH_2 arising from Rh (^4F) + H_2 and Rh (^2F) + H_2. They found that the Rh (^2F) atom inserts into H_2 spontaneously while the Rh (^4F) state has to surmount a large barrier of 56 kcal/mol. The ground state of RhH_2 was found to be a $^2A_1$ state with $r_e = 1.51$ Å and $\theta_e = 83°$. The $^2A_1$ state was found to be 10 kcal/mol more stable than Rh (^4F) + H_2. The spin–orbit contaminations of different states of RhH_2 were found to be quite small.

A few dramatic differences are noticed in comparing RhH_2 with IrH_2. First, the barrier for the insertion of Rh (^4F) into H_2 (56 kcal/mol) is substantially larger than the barrier for the insertion of Ir (^4F) into H_2 (~28 kcal/mol). The spin–orbit coupling of the quartet and doublet states near the crossing region provide nonzero transition probability for the quartet states to hop to the doublet states and vice versa thereby reducing the barrier further to less than 4 kcal/mol while such spin–orbit coupling was found to be very small for RhH_2. Consequently, the Rh atom is found to be much less reactive to H_2 compared to the Ir atom.

The stability of IrH_2 ($^2A_1$) relative to Ir (^4F) + H_2 is 28 kcal/mol in the absence of spin–orbit coupling compared to only 10 kcal/mol for RhH_2 although the latter value is at the CAS level. Even if improvements from higher-order correlations are taken into consideration for RhH_2 up to 7 kcal/mol, evidently, IrH_2 is considerably more stable than RhH_2. Note that the IrH_2 E state is 27 kcal/mol relative to Ir ($^4F_{9/2}$) + H_2 including spin–orbit coupling. The enhanced stability of IrH_2 relative to Ir + H_2 would make it a more attractive candidate for experimental studies since it will have long enough lifetimes to be seen in a supersonic beam.

The spin–orbit effects are substantially larger for IrH_2 compared to RhH_2. The spin–orbit contamination of different states of RhH_2 was found to be at most 1% while the spin–orbit contamination for IrH_2 was found to add up to 25%–30%. Hence, spin–orbit effects are dramatically larger for IrH_2. As noted before, a major contribution of spin–orbit coupling is to the H–Ir–H bond angle of the ground state which changes by 9°.

The dipole moment of the ground state of RhH_2 is 2.67 D with Rh^+H^- polarity compared to 2.2 D for IrH_2 with the same polarity. The dipole moments of the two species are comparable since the M–H bond lengths for IrH_2 and RhH_2 are 1.545 and 1.54 Å, respectively. The $^2A_1$ state of RhH_2 has a smaller bond angle (84°) compared to IrH_2 (92°). But this difference seems to compensate for the more ionicity of the Ir–H bonds so that the dipole moments become comparable. However, the spin–orbit effects have larger impact on the dipole moment of IrH_2 compared to RhH_2.

We conclude that the main difference between RhH_2 and IrH_2 is in the reactivity and stability. The Ir atom is more reactive and forms more stable Ir–H bonds in the ground state of IrH_2. The other important contrasts are in the dramatically larger spin–orbit effects which change the bond angles and enhance the nonadiabatic transition probability for the insertion of Ir (^4F) state into H_2.

VI. CONCLUSION

The PES of IrH_2 and IrH_2^+ arising from Ir (^4F) + H_2, Ir (^2F) + H_2, Ir (^4F) + H + H, Ir^+ (^5D) + H_2, Ir^+ (^3F) + H_2, and Ir^+ (^1G) + H_2 dissociation limits were studied using a complete active space MCSCF (CAS-MCSCF) followed by MRCI and RCI calculations. The ground state of IrH_2 including spin–orbit effects is found to be a $E(I)$ ($^2A_1$) state with $r_e = 1.54$ Å, $\theta_e = 92°$ and $D_e = 27$ kcal/mol relative to Ir ($^4F_{9/2}$) + H_2. The Ir (^4F) atom has to surmount a barrier for insertion into H_2 while the Ir (^2F) atom spontaneously inserts into H_2 in the absence of spin–orbit coupling. However, spin–orbit coupling of the quartet and doublet surfaces near the curve crossing region reduced the barrier for insertion of Ir (^4F) into H_2 substantially to 5 kcal/mol through nonvanishing nonadiabatic transition probability facilitated by the spin–orbit coupling. Therefore, we find Ir (^4F) to be more reactive through spin–orbit coupling.

The spin–orbit effects were found to be significant for both IrH_2 and IrH_2^+. The $E(I)$ ($^2A_1$) ground state of IrH_2 was found to be 63% $^2A_1$, 16% $^2B_1$, and 17% $^2A_2$ while the $^3A_2$ (A_1) ground state of IrH_2^+ was found to be 63% $^3A_2$, 15% $^3B_2$, 12% $^3B_1$, and 7% $^1A_1$. This large spin–orbit mixing induces dramatic changes in the ground state θ_e's of the two species (9.5°).

The Ir^+ (^5D) state has to surmount a barrier for insertion into H_2 in the absence of spin–orbit coupling while both Ir^+ (^3F) and Ir^+ (^1G) states insert into H_2 spontaneously. The crossing of quintet surfaces with triplet surfaces reduce the barrier for Ir^+ (^5D) into H_2 through spin–orbit coupling of the two surfaces significantly to ~5 kcal/mol, thereby providing nonzero nonadiabatic transition probability for the ground state of Ir^+ to insert into H_2. The IrH_2^+ ion in its $^3A_2$ (A_1) ground state was found to be 30 kcal/mol more stable than $Ir^+ + H_2$.

The saddle points in some of the quartet states of IrH_2 and all quintet states of IrH_2^+ were found to arise from several avoided crossings. Both IrH_2 and IrH_2^+ states exhibit complex $6s6p5d$ hybridization as evidenced from their Mulliken populations.

It is concluded that the Ir atom reacts more readily with H_2 compared to Rh. The stability of IrH_2 is also considerably more than RhH_2.

ACKNOWLEDGMENTS

This research was supported by the Department of Energy under Grant No. DEFG02-86ER-13558. Dingguo Dai thanks Department of Chemistry, Tongji University, Shanghai, People's Republic of China, for providing a leave which made this joint study possible.

[1] R. E. Smalley, in *Comparison of ab initio Quantum Chemistry with Experiment*, edited by R. J. Bartlett (Reidel, New York, 1985), pp. 53–65; J. Allison, Prog. Inorg. Chem. **34**, 627 (1986); S. W. McElvany and J. Allison, Organometalics **5**, 1219 (1986).
[2] P. B. Armentrout and J. L. Beauchamp, Acc. Chem. Res. **22**, 315 (1989); N. Aristov and P. B. Armentrout, J. Am. Chem. Soc. **108**, 1806 (1986).
[3] R. Crabtree, Acc. Chem. Res. **23**, 95 (1990); G. J. Kubas, *ibid.* **21**, 120 (1988).
[4] R. J. Van Zee, T. C. Devore, J. L. Wilkerson, and W. Weltner, Jr., J. Chem. Phys. **69**, 1869 (1978); R. J. Van Zee, T. C. Devore, and W. Weltner, Jr., *ibid.* **71**, 2051 (1979); R. J. Van Zee, D. A. Garland, and W. Weltner, Jr., *ibid.* **85**, 3237 (1986).
[5] P. B. Armentrout, L. F. Halle, and J. L. Beauchamp, J. Am. Chem. Soc. **103**, 6501 (1981); J. L. Elkind and P. B. Armentrout, J. Chem. Phys. **86**, 1868 (1987); L. Sunderlin, N. Aristov, and P. B. Armentrout, J. Am. Chem. Soc. **109**, 78 (1987); J. L. Elkind, L. Sunderlin, and P. B. Armentrout, J. Phys. Chem. **93**, 3151 (1989).
[6] J. L. Elkind and P. B. Armentrout, Inorg. Chem. **25**, 1078 (1986).
[7] S. C. Richtsmeier, E. K. Parks, K. Liu, L. G. Pobo, and S. J. Riley, J. Chem. Phys. **82**, 3659 (1985); K. Liu, E. K. Parks, S. C. Richtsmeier, L. G. Pobo, and S. J. Riley, *ibid.* **83**, 5353 (1985).
[8] M. D. Morse, M. E. Geusic, J. R. Heath, and R. E. Smalley, J. Chem. Phys. **83**, 2293 (1985); M. E. Geusic, M. D. Morse, and R. E. Smalley, Rev. Sci. Instrum. **56**, 2123 (1985); J. Chem. Phys. **82**, 590 (1985); J. M. Alford, F. D. Weiss, R. T. Laaksonen, and R. E. Smalley, J. Phys. Chem. **90**, 4480 (1986); J. L. Elkind, F. D. Weiss, J. M. Alford, R. T. Laaksonen, and R. E. Smalley, J. Chem. Phys. **88**, 5215 (1988).
[9] R. L. Whetten, D. M. Cox, D. J. Trevor, and A. Kaldor, Phys. Rev. Lett. **54**, 1494 (1985); R. L. Whetten, M. R. Zakin, D. M. Cox, D. J. Trevor, and A. Kaldor, J. Chem. Phys. **85**, 1697 (1986).
[10] L. B. Knight, Jr., S. T. Cobranchi, J. Herlong, T. Kirk, K. Balasubramanian, and K. K. Das, J. Chem. Phys. **92**, 2721 (1990); T. D. Varberg, R. W. Field, and A. J. Merer, *ibid.* **92**, 7123 (1990).
[11] Z. Knor, in *Catalysis: Science and Technology*, edited by J. R. Angerson and M. Boudart (Springer, Berlin, 1982), Vol. 3, p. 23.
[12] M. Krauss and W. J. Stevens, Annu. Rev. Phys. Chem. **35**, 357 (1984); P. A. Christiansen, W. C. Ermler, and K. S. Pitzer, *ibid.* **36**, 407 (1985); K. Balasubramanian and K. S. Pitzer, Adv. Chem. Phys. **67**, 287 (1987).
[13] K. Balasubramanian, J. Phys. Chem. **93**, 6585 (1989).
[14] K. K. Das and K. Balasubramanian, J. Chem. Phys. **91**, 2433 (1989).
[15] K. Balasubramanian, J. Chem. Phys. **87**, 2800 (1987); J. J. Low and W. A. Goddard III, Organometallics **5**, 609 (1986); E. Poulain, J. Garcia-Prieto, M. A. Ruiz, and O. Novaro, Int. J. Quantum Chem. **29**, 1181 (1986).
[16] K. Balasubramanian and M. Z. Liao, J. Phys. Chem. **92**, 4595 (1988).
[17] K. K. Das and K. Balasubramanian, J. Chem. Phys. **92**, 6697 (1990).
[18] R. Eisenberg and B. J. Fisher, Ann. N. Y. Acad. Sci. **415**, 65 (1983); D. Milstein and J. C. Calabrese, J. Am. Chem. Soc. **104**, 3773 (1982).
[19] R. H. Crabtree, D. R. Anton, and M. W. Davis, Ann. N. Y. Acad. Sci. **415**, 268 (1983); D. R. Anton and R. H. Crabtree, Organometallics **2**, 621 (1983).
[20] H. D. Empsall, E. Mentzer, and B. L. Shaw, J. Chem. Soc. Chem. Commun. **1975**, 861.
[21] J. M. Brown, P. A. Chaloner, G. Descotes, R. Glaser, D. Lafont, and D. Sinou, J. Chem. Soc. Chem. Commun. **1979**, 611.
[22] M. D. Ward, T. V. Harris, and J. Schwartz, J. Chem. Soc. Chem. Commun. **1980**, 357.
[23] R. B. Ross, J. M. Powers, T. Atashroo, W. C. Ermler, L. A. LaJohn, and P. A. Christiansen, J. Chem. Phys. (in press).
[24] K. Balasubramanian, J. Z. Wang, and K. K. Das, Mol. Phys. **69**, 147 (1990).
[25] K. Balasubramanian and J. Z. Wang, J. Chem. Phys. **91**, 7761 (1989).
[26] K. Balasubramanian, J. Chem. Phys. **88**, 5731 (1988).
[27] R. M. Pitzer and N. W. Winter, J. Phys. Chem. **92**, 3061 (1988).
[28] The major authors of the ALCHEMY II codes are B. Liu, M. Yoshimine, and B. Lengsfield.
[29] K. Balasubramanian, Chem. Phys. Lett. **127**, 585 (1986).
[30] R. M. Pitzer, ARGOS, Integral codes.
[31] P. J. Hay and W. R. Wadt, J. Chem. Phys. **82**, 270 (1985); W. R. Wadt and P. J. Hay, *ibid.* **82**, 284, 299 (1985).
[32] C. E. Moore, *Atomic Energy Levels* (National Bureau of Standards, Washington, D. C., 1971), Vol. 2.
[33] H. Eyring, J. Walter, and G. E. Kimball, *Quantum Chemistry* (Wiley, New York, 1944).
[34] K. Balasubramanian and D. W. Liao, J. Phys. Chem. **92**, 6259 (1988).